

# Adiabatic Shear Susceptibility of Fe<sub>50</sub>Mn<sub>30</sub>Co<sub>10</sub>Cr<sub>10</sub> High-Entropy Alloy



SHUANGJUN YANG, YANG YANG, ZHIYU YANG, CHI LU, and WENHUI LIU

Dynamic loading of the Fe<sub>50</sub>Mn<sub>30</sub>Co<sub>10</sub>Cr<sub>10</sub> high-entropy alloy (HEA) was carried out using a split Hopkinson pressure bar at room temperature. The effects of microstructures and loading strain rates on the adiabatic shear susceptibility of an Fe<sub>50</sub>Mn<sub>30</sub>Co<sub>10</sub>Cr<sub>10</sub> HEA were evaluated for the first time by comparing metallographic observation, the stress collapse time, the critical values of strain corresponding to the adiabatic shearing initiation, and the adiabatic shearing formation energy per unit volume. The results show that the adiabatic shear susceptibility increases with the increase of loading strain rate. The smaller the grain size and the more hexagonal close-packed (hcp) phase of the Fe<sub>50</sub>Mn<sub>30</sub>Co<sub>10</sub>Cr<sub>10</sub> HEA, the greater the strain hardening effect and the stronger the localized deformation resistance under the same dynamic loading conditions, and the lower the adiabatic shear susceptibility.

<https://doi.org/10.1007/s11661-020-05641-3>

© The Minerals, Metals & Materials Society and ASM International 2020

## I. INTRODUCTION

CONTINUOUS development of compositions, microstructures, and mechanical properties in the high-entropy alloys (HEAs) has been shown since the concept of HEA was put forward.<sup>[1–6]</sup> In the original HEAs design, the standard of mixing five or more elements in equiatomic or near equiatomic concentrations were strictly adhered to maximize the entropy value of the HEA.<sup>[1–6]</sup> However, research has found that the maximization of configurational entropy in equiatomic HEAs is not the decisive factor for the formation of a solid solution phase.<sup>[7,8]</sup> The observation has motivated the design of novel non-equiatomic HEA systems and relaxed the limitation on the composition elements of HEAs. HEAs with non-equal molar fractions<sup>[9,10]</sup> or less than five elements<sup>[11,12]</sup> gradually appeared. A dual-phase Fe<sub>50</sub>Mn<sub>30</sub>Co<sub>10</sub>Cr<sub>10</sub> HEA with high strength and ductility resulting from Transformed Induced Plasticity (TRIP) effect was designed by Li

*et al.*<sup>[13]</sup> The design concept of Transformation Induced Plasticity-assisted, Dual-Phase HEA (TRIP-DP-HEA) provides a new research direction for the design and performance optimization of HEAs.

Adiabatic shearing is a phenomenon of thermal-viscoplastic constitutive instability of materials under high strain rate loading.<sup>[14]</sup> It is commonly found in dynamic deformation processes involving high strain rate loading, such as explosions, penetrations, and high-speed impacts. At present, adiabatic shearing behavior of many materials has been reported, involving metals, polymers, and composites, such as stainless steels,<sup>[15–17]</sup> aluminum alloys,<sup>[18,19]</sup> titanium and titanium alloys,<sup>[20–24]</sup> magnesium alloys,<sup>[25–29]</sup> tungsten alloys,<sup>[30]</sup> polycarbonates,<sup>[31]</sup> SiC<sub>p</sub> particle-reinforced 2024 Al composites,<sup>[32]</sup> and so on. Adiabatic shear susceptibility is used to characterize the degree of difficulty in the occurrence of adiabatic shearing. The higher the adiabatic shear susceptibility, the more likely adiabatic shearing will occur. The main influencing factors of adiabatic shear susceptibility include the structure and state factors of materials (sample shape, material composition, phase composition, grain size, heat treatment state, *etc.*), and the external loading conditions (strain rate, deformation degree, deformation temperature, stress state, *etc.*). Researchers show that the adiabatic shear susceptibility of materials possessing different microstructures varies greatly.<sup>[26,33–35]</sup> In addition, the adiabatic shear susceptibility increases with the increase of strain rate and strain.<sup>[34,36,37]</sup>

At present, research on HEAs has mainly focused on the microstructure and mechanical properties of alloys under quasi-static deformation conditions, and there are limited studies on their dynamic behaviors. The main

---

SHUANGJUN YANG is with the School of Material Science and Engineering, Central South University, Changsha 410083, China and also with the School of Material Science and Engineering, Hunan University of Science and Technology, Xiangtan 411201, China. YANG YANG is with the School of Material Science and Engineering, Central South University and also with the Key Laboratory of Ministry of Education for Nonferrous Metal Materials Science and Engineering, Central South University, Changsha 410083, China. Contact e-mails: yangyang@csu.edu.cn, yangyanggroup@163.com ZHIYU YANG and CHI LU are with the School of Material Science and Engineering, Central South University. WENHUI LIU is with the School of Material Science and Engineering, Hunan University of Science and Technology.

Manuscript submitted July 9, 2019.

Article published online January 23, 2020

related researches are as follows: Kumar *et al.*<sup>[38]</sup> studied the Al<sub>0.1</sub>CrFeCoNi alloy and found that the HEA did not show a thermal softening effect when the strain rate reached the order of 10<sup>4</sup>s<sup>-1</sup> and thought that the HEA had a high susceptibility to strain hardening rate. Li *et al.*<sup>[39]</sup> found that no adiabatic shear band was formed in the Al<sub>0.3</sub>CoCrFeNi HEA under the loading condition of 1800s<sup>-1</sup> at different temperatures. Li *et al.*<sup>[40]</sup> studied the adiabatic shearing behavior of the CrMnFeCoNi HEA and found that an adiabatic shear band was formed when the shear strain was greater than 7 at the strain rate of 10<sup>4</sup> s<sup>-1</sup>. It can be seen that the current studies show that HEAs have relatively low adiabatic shear susceptibility.

The fundamental purpose of studying adiabatic shearing is to optimize material structure design, improve dynamic performance, and control (restraint/promote) adiabatic shearing to provide scientific guidance for the service safety of materials under dynamic loading. The Fe<sub>50</sub>Mn<sub>30</sub>Co<sub>10</sub>Cr<sub>10</sub> HEA has the advantages of high strength and good ductility, and it has a good application prospect in high-speed kinetic energy weapon materials, future nuclear energy, and space protection materials, *etc.* However, at present, there are few studies on the Fe<sub>50</sub>Mn<sub>30</sub>Co<sub>10</sub>Cr<sub>10</sub> HEA, and no literature has been reported on the adiabatic shearing behavior of the Fe<sub>50</sub>Mn<sub>30</sub>Co<sub>10</sub>Cr<sub>10</sub> HEA. Therefore, it is of great theoretical and engineering significance to study the adiabatic shear susceptibility of the Fe<sub>50</sub>Mn<sub>30</sub>Co<sub>10</sub>Cr<sub>10</sub> HEA.

The effects of microstructures and loading strain rates on the adiabatic shear susceptibility of the Fe<sub>50</sub>Mn<sub>30</sub>Co<sub>10</sub>Cr<sub>10</sub> HEA were explored for the first time in this paper, which provide experimental data and theoretical support for the engineering application of this alloy.

## II. EXPERIMENTAL MATERIALS AND METHODS

The Fe<sub>50</sub>Mn<sub>30</sub>Co<sub>10</sub>Cr<sub>10</sub> (at. pct) HEA ingot was cast in a vacuum induction furnace using pure metals (purity higher than 99.8 wt pct) with predetermined compositions as designed by Li *et al.*<sup>[13]</sup> The as-cast ingot size was 100 × 100 × 35 mm<sup>3</sup>. The element content of the as-cast ingot was determined by Inductively Coupled Plasma Optical Emission Spectrometer (ICP-OES). The results are presented in Table I. The actual composition is close to the designed composition. The as-cast sample consists of  $\gamma$ -fcc (face-centered cubic) phase and lamellar  $\epsilon$ -hcp (hexagonal close-packed) phase, and the detailed analysis was shown in Reference 41.

**Table I. Measured Chemical Composition of the Fe<sub>50</sub>Mn<sub>30</sub>Co<sub>10</sub>Cr<sub>10</sub> (At. Pct) HEA**

	Fe	Mn	Co	Cr
Theoretical Composition (At. Pct)	50	30	10	10
Actual Composition (At. Pct)	50.44	30.04	9.71	9.81

The following deformation and heat treatment were done after casting: (1) the as-cast sample was firstly annealed at 1173 K for 1 hour, then rolled in five passes at 1173 K (50 pct thickness reduction), and subsequently air cooled. The hot-rolled sample was annealed at 1273 K for 2 hours in Ar atmosphere, followed by water quenching (The as-cast sample was hot rolled and annealed, followed by water quenching, HRQ); (2) The HRQ sample was cold rolled in eight passes (40 pct thickness reduction). The cold-rolled sample was annealed at 1273 K for 2 hours in Ar atmosphere, followed by water quenching (The HRQ sample was cold rolled and annealed, followed by water quenching, CRQ).

Forced shear is one of the common methods to study adiabatic shearing failure by using a split Hopkinson compression bar (SHPB)-loaded hat-shaped sample. Stress concentration area is created through geometrical discontinuity of the cylindrical hat-shaped sample to control the starting position of shear localization and the direction of shear band extension, thus achieving the purpose of studying adiabatic shearing behavior. The impact rod, the incident rod, and the transmission rod are all no. 45 steel and they all have the same diameter of 16 mm. The length of the impact rod is 210 mm, and the length of the incident rod and the transmission rod both are 1200 mm. The loading pressure is controlled to obtain different loading rates. The experimental temperature is 298 K. The width and length of the designed shear band of the hat-shaped sample are 0.1 and 3 mm, respectively. The sample placement diagram and sample size diagram are shown in Figure 1. Electrical signals are obtained by strain gauges attached to the incident rod and the transmission rod during loading process. The core of the SHPB experiment is based on two assumptions: the one-dimensional stress wave assumption and the specimen uniformity assumption. The one-dimensional stress wave assumption means that the sample is in a one-dimensional stress state during deformation. The specimen uniformity assumption means that the stress on both sides of the specimen is assumed to be an equilibrium state. Based on the above two assumptions, the stress-strain curve of the hat-shaped sample can be obtained by the following equations<sup>[37]</sup>:

$$\tau = \frac{E_0 A_s \varepsilon_t(t)}{\pi h \left( \frac{d_i + d_c}{2} \right)} \quad [1]$$

$$\dot{\gamma} = \frac{2C_0 [\varepsilon_i(t) - \varepsilon_t(t)]}{s} \quad [2]$$

$$\gamma = \frac{2C_0 \int_0^t [\varepsilon_i(t) - \varepsilon_t(t)] dt}{s} \quad [3]$$

$$\sigma = 2\tau \quad [4]$$

$$\varepsilon = \ln \sqrt{1 + \gamma + \frac{\gamma^2}{2}}, \quad [5]$$

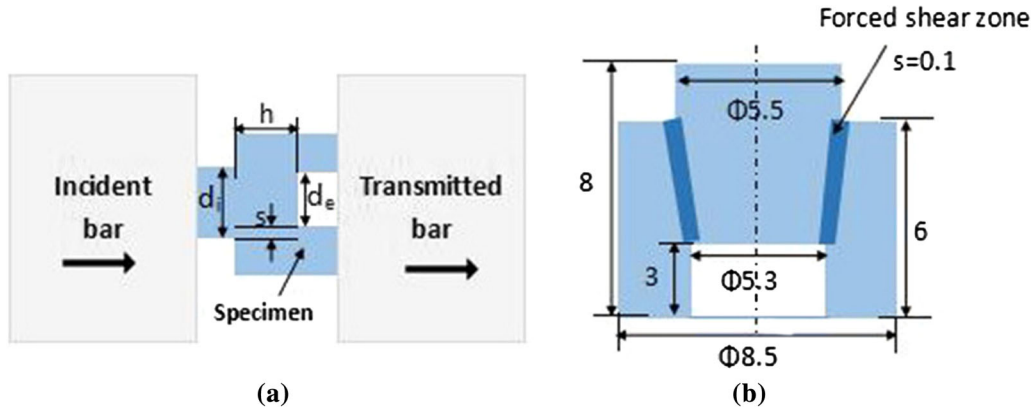


Fig. 1—Schematic diagram of sample placement and size: (a) sample placement position; (b) sample size (unit: mm).

where  $\tau$  is the shear stress,  $\dot{\gamma}$  is the strain rate.  $\gamma$  is the shear strain,  $\sigma$  is the true stress,  $\varepsilon$  is the true strain,  $E_0$  is the elastic modulus of bar ( $E_0 = 200$  GPa),  $C_0$  is the longitudinal wave velocity ( $C_0 = 5000$  m/s), seconds and hours are the length and width of the shear band,  $d_i$  and  $d_e$  are the geometrical parameters of the hat-shaped specimen, as shown in Figure 1, and  $\varepsilon_i(t)$  and  $\varepsilon_t(t)$  are reflected and transmitted wave signals on the bars; their units are all millivolt (mV), and  $t$  is the deformation time. When the sample is loaded by the SHPB, the electrical signal curves ( $\varepsilon_i(t)$  and  $\varepsilon_t(t)$ ) can be directly obtained. The loading curves can then be obtained by Eqs. [1] through [5] with Origin software. The loading strain rate of SHPB is generally  $10^3$  to  $10^4$   $s^{-1}$ . However, this design aims to make the loading strain rate reach  $10^5$   $s^{-1}$  to obtain an adiabatic shear band. According to Eq. [3], the smaller the width of the shear band, the higher the loading strain rate. The ultimate width of the designed shear band is  $s = 0.1$ mm. The final loading strain rates calculated in this paper were about  $1.37 \times 10^5$ ,  $1.55 \times 10^5$ , and  $1.61 \times 10^5$   $s^{-1}$ .

The X-ray diffraction (XRD) was carried out on a Rigaku SmartLab diffractometer operating at 40 kV and 30 mA with Cu  $K_\alpha$  radiation (wavelength:  $\lambda = 0.15418$  nm), and a scanning angle of 10 to 100 deg with a scanning step of degrees per minute.

Rietveld refinement of the XRD data was performed to quantify the hcp phase fraction using Jade software. The scale factors of individual phases were computed by the minimization of R factor given by Eq. [6]<sup>[42]</sup>:

$$R = \frac{\sum_P w_p (I_p^{avr} - I_p^{cal})^2}{\sum_P w_p (I_p^{cal})^2}, \quad [6]$$

where  $w_p = \frac{1}{I_p^{avr}}$  is weight factor, p is the diffraction peak of  $\varepsilon$ -hcp phase or  $\gamma$ -fcc phase,  $I_p^{cal} = mSLPF$  is the calculated intensity for particular diffraction, where m is the multiplicity factor, S is the scale factor, L is the Lorentz factor, P is the polarization factor, and F is the structure factor. The weight fractions were computed from refined scale factors according to Eq. [7]<sup>[42]</sup>:

$$W_a = \frac{(SZMV)_a}{\sum_i (SZMV)_i}, \quad [7]$$

where S is the scale factor, Z is the number of formula units per unit cell, M is the mass of the formula unit, and V is the unit cell volume. The above parameters are automatically obtained by Rietveld process.

Samples for microstructure observation were cut from the dynamically deformed hat-shaped samples along the loading axis by wire-electrode cutting. Specimens were prepared by standard mechanical polishing and then etched in aqua regia, and finally observed under a POLYVAR-MET metallographic microscope after 10 seconds of etching. The metallographic photographs were taken to analyze grain size and width of the adiabatic shear band by image pro plus software.

### III. RESULTS AND DISCUSSIONS

#### A. The Microstructures of Alloy Before Loading

The initial morphological characteristics of samples are shown in Figure 2. Figures 2(a) and (c) are the morphological characteristics of the HRQ sample and the corresponding XRD normalized pattern. Figures 2(b) and (d) are the morphological characteristics of the CRQ sample and the corresponding XRD normalized pattern. It can be seen from Figure 2 that both samples consist of  $\gamma$  phase (face-centered cubic (fcc),  $a = 3.618$  Å) and lamellar  $\varepsilon$  phase (hcp,  $a = 2.529$  Å,  $c = 4.130$  Å).<sup>[13]</sup> The average grain size of the HRQ sample is about 35  $\mu$ m, while that of the CRQ sample is about 10  $\mu$ m. As shown in Figures 2(c) and (d), the diffracted intensity of  $\gamma$  (220) and  $\gamma$  (311) in the CRQ sample is slightly increased and that of  $\varepsilon$  (002) and  $\varepsilon$  (101) is largely increased compared to that of the HRQ sample. The diffraction intensity of the  $\varepsilon$  phase in the CRQ sample is relatively increased. The hcp phase content of the HRQ sample is measured about 28.3 wt pct, while that of the CRQ sample is measured about 46.0 wt pct by XRD Rietveld analysis results.



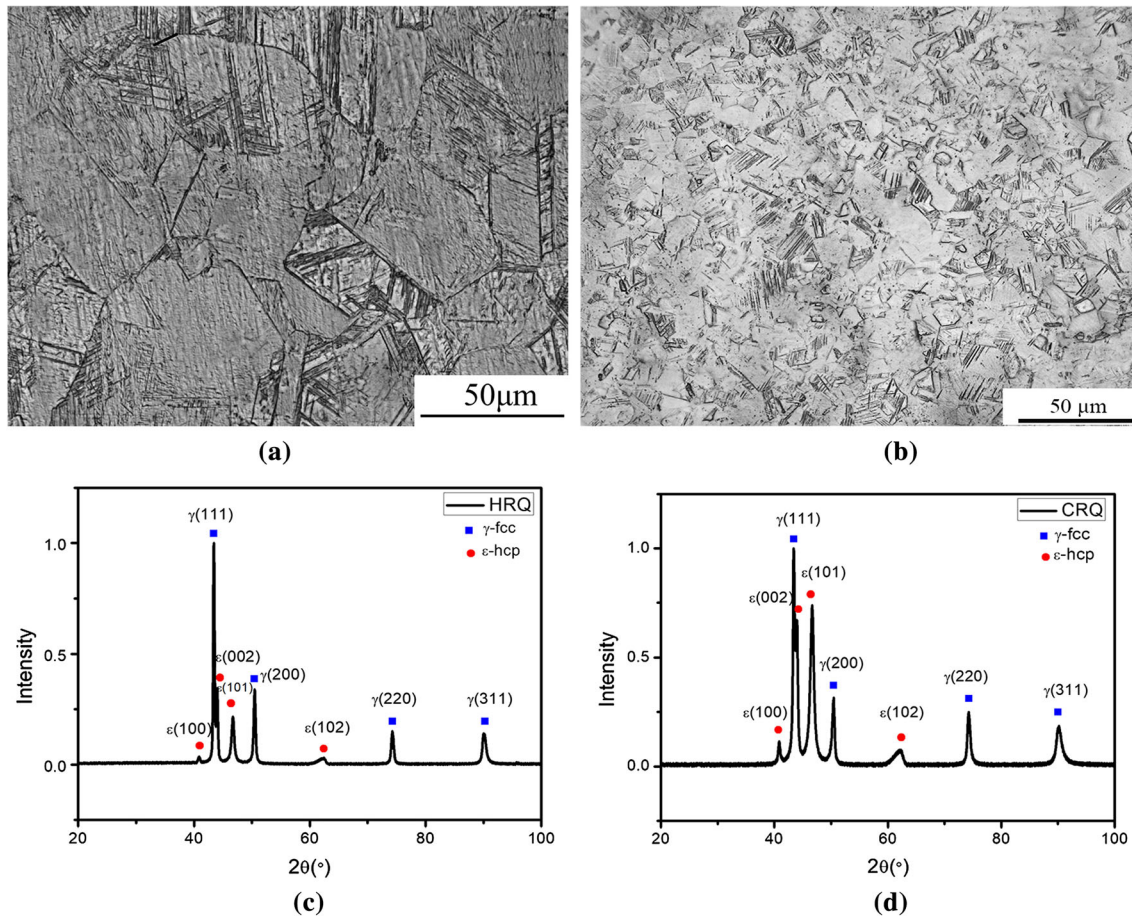


Fig. 2—The morphological characteristics of samples and corresponding pattern of XRD: (a) morphological characteristics of the HRQ sample; (b) metallographic morphology of the CRQ sample; (c) XRD pattern of the HRQ sample; (d) XRD pattern of the CRQ sample.

### B. The Adiabatic Shear Susceptibility of $Fe_{50}Mn_{30}Co_{10}Cr_{10}$ HEA

The adiabatic shear susceptibility of samples possessing different microstructures under the same dynamic loading condition can be compared by the stress collapse time, the critical strain corresponding to the adiabatic shearing initiation, the adiabatic shearing formation energy, and the metallographic observation. Generally speaking, the shorter the stress collapse time and the smaller the critical strain when adiabatic shearing occurs, indicating that the higher the adiabatic shear susceptibility of the sample. In addition, the less energy absorbed when adiabatic shearing occurs, the easier it is to form an adiabatic shear band. The adiabatic shearing formation energy per unit volume can be calculated as follows<sup>[33]</sup>:

$$E = \int_0^{\varepsilon} \sigma d\varepsilon, \quad [8]$$

where  $\sigma$  is the true stress, and  $\varepsilon$  is the true strain. According to Eq. [8], the adiabatic shearing formation energy per unit volume can be obtained by integrating the starting point of the stress–strain curve to the point where adiabatic shearing appears, namely “stress collapse point.”

Below the effects of microstructures and loading strain rates on the adiabatic shear susceptibility of  $Fe_{50}Mn_{30}Co_{10}Cr_{10}$  HEA were analyzed from two aspects. On the one hand, the morphological characteristics of samples possessing different microstructures under different loading strain rates were analyzed. On the other hand, the collapse time, the critical strain when adiabatic shearing occurs, and the adiabatic shearing formation energy per unit volume of samples possessing different microstructure under different loading strain rates were compared.

#### 1. Effects of microstructures on the adiabatic shear susceptibility

*a. Under the loading strain rate of  $1.37 \times 10^5 \text{ s}^{-1}$*  As shown in Figure 3, no adiabatic shear band was formed in both samples under the loading strain rate of  $1.37 \times 10^5 \text{ s}^{-1}$ . Adiabatic shearing localization appeared near the hat port of the HRQ sample (Figure 3(a)) but did not develop into an adiabatic shear band. However, there was no tendency of adiabatic shearing localization near the hat port of the CRQ sample (Figure 3(b)). It can be seen that the adiabatic shear susceptibility of the HRQ sample is higher than that of the CRQ sample. As shown in Figures 3(c) and

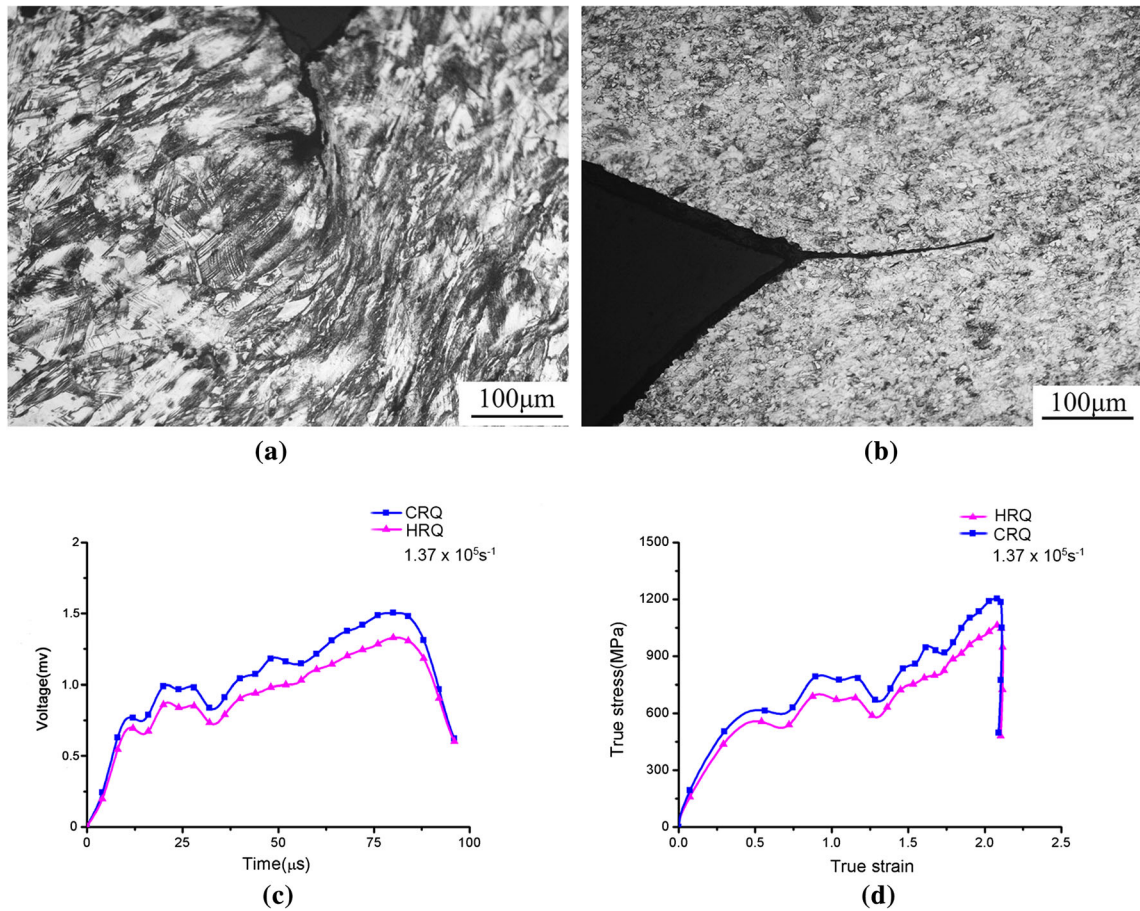


Fig. 3—The comparison of morphological characteristics, loading curves of both samples under the loading strain rate of  $1.37 \times 10^5 \text{ s}^{-1}$ : (a) the HRQ sample; (b) the CRQ sample; (c) voltage–time loading curves; (d) true stress–true strain curves.

(d), there was no stress collapse point in both samples, and it can be seen from the true stress–true strain curves that the deformation process mainly includes three stages. Firstly, the stress increases with the increase of strain. Then, the stress has a fluctuate increase with the increase of strain, which is the result of continuous competition between strain hardening and thermal softening, and finally strain hardening exceeds thermal softening. Finally, the stress drops sharply, which is the unloading stage.

*b. Under the loading strain rate of  $1.55 \times 10^5 \text{ s}^{-1}$*  Figure 4 shows the comparison of morphological characteristics, loading curves, and adiabatic shearing formation energy per unit volume of samples under the loading strain rate of  $1.55 \times 10^5 \text{ s}^{-1}$ . It can be seen that a transformed adiabatic shear band was formed in both samples, as shown in Figures 4(a) through (d). Figures 4(a) and (c) show that the actual average width of the adiabatic shear band in the HRQ sample is about  $18.1 \mu\text{m}$ . Figures 4(b) and (d) show that the actual average width of the adiabatic shear band in the CRQ sample is about  $2.6 \mu\text{m}$ . As seen in Figures 4(e) and (f), there was a stress collapse point in both samples (points a1/a2 in Figures 4(e) and b1/b2 in (f)). The parameters that characterize the adiabatic shear susceptibility under

the loading strain rate of  $1.55 \times 10^5 \text{ s}^{-1}$  were obtained according to Figure 4, as shown in Table II. It can be seen from Table II that stress collapse appears earlier in the HRQ sample under the loading strain rate of  $1.55 \times 10^5 \text{ s}^{-1}$ . The critical strain and the adiabatic shearing formation energy per unit volume of the HRQ sample decreased compared to that of the CRQ sample. Therefore, the adiabatic shear susceptibility of the HRQ sample is higher than that of the CRQ sample.

*c. Under the loading strain rate of  $1.61 \times 10^5 \text{ s}^{-1}$*  Figure 5 shows the comparison of morphological characteristics, loading curves, and adiabatic shearing formation energy of both samples under the loading strain rate of  $1.61 \times 10^5 \text{ s}^{-1}$ . It can be seen from Figures 5(a) and (b) that the adiabatic shear band of both samples was developed to mature, and a very wide of crack was generated. The crack penetrated the shear direction of the HRQ sample (Figure 5(a)), while the crack length of the CRQ sample is shorter than that of the HRQ sample (Figure 5(b)). The actual average width of the adiabatic shear band in the CRQ sample is about  $14.9 \mu\text{m}$ . The parameters that characterize the adiabatic shear susceptibility under the loading strain rate of  $1.61 \times 10^5 \text{ s}^{-1}$  were obtained according to Figure 5, as shown in Table III. It can be seen from



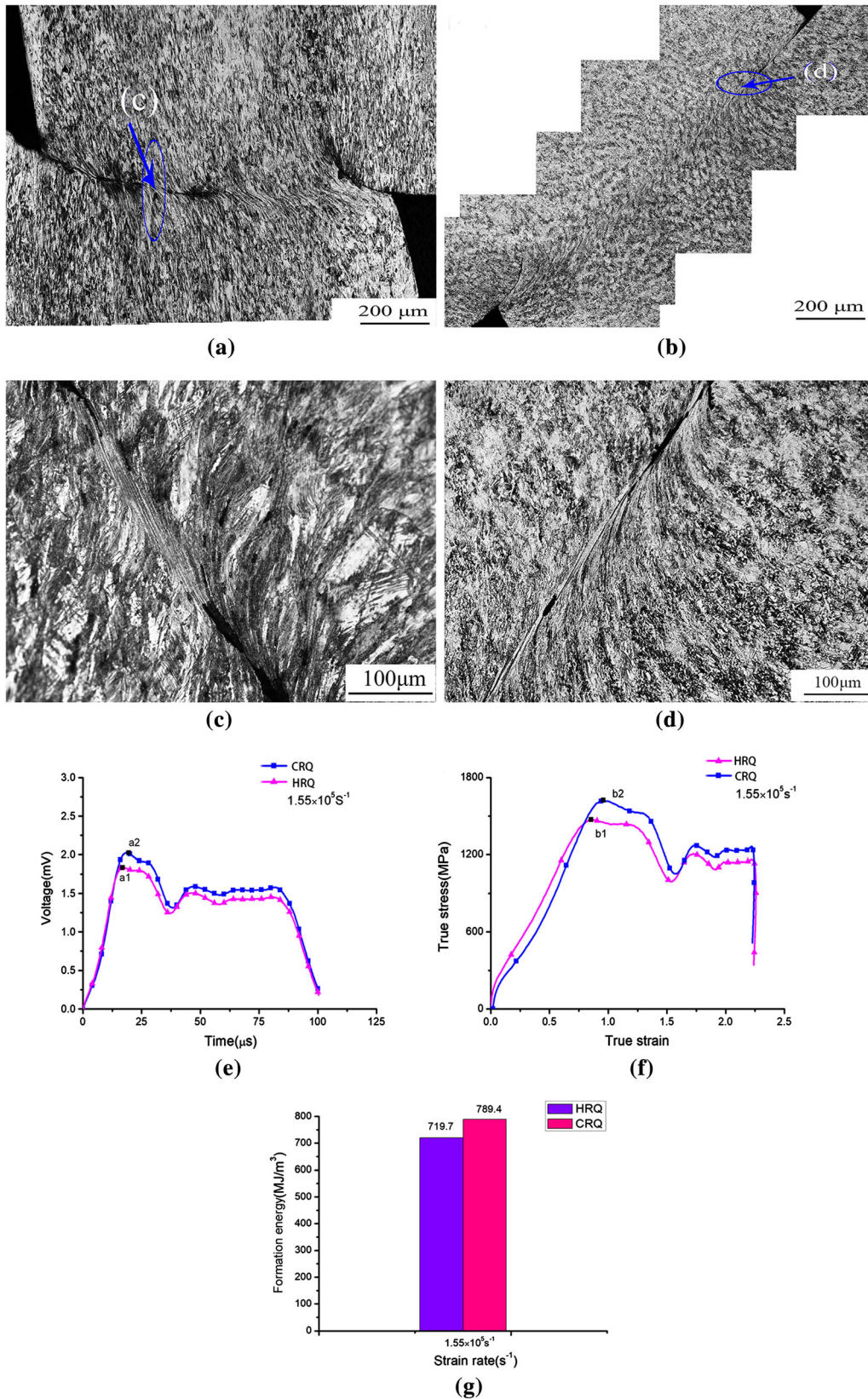


Fig. 4—The comparison of morphological characteristics, loading curves, and formation energy of adiabatic shearing per unit volume of both samples under the loading strain rate of  $1.55 \times 10^5 \text{ s}^{-1}$ : (a) the HRQ sample; (b) the CRQ sample; (c) (a) local magnification; (d), (b) local magnification; (e) voltage–time loading curves; (f) true stress–true strain curves; (g) comparison of adiabatic shearing formation energy per unit volume.

**Table II. Parameters Characterizing the Adiabatic Shear Susceptibility Under the Loading Strain Rate of  $1.55 \times 10^5 \text{ s}^{-1}$**

	Loading Strain Rate ( $\text{s}^{-1}$ )	Stress Collapse Time ( $\mu\text{s}$ )	Critical Strain	Formation Energy ( $\text{MJ}/\text{m}^3$ )
HRQ	$1.55 \times 10^5$	16.9	0.85	719.7
CRQ	$1.55 \times 10^5$	19.2	0.95	789.4

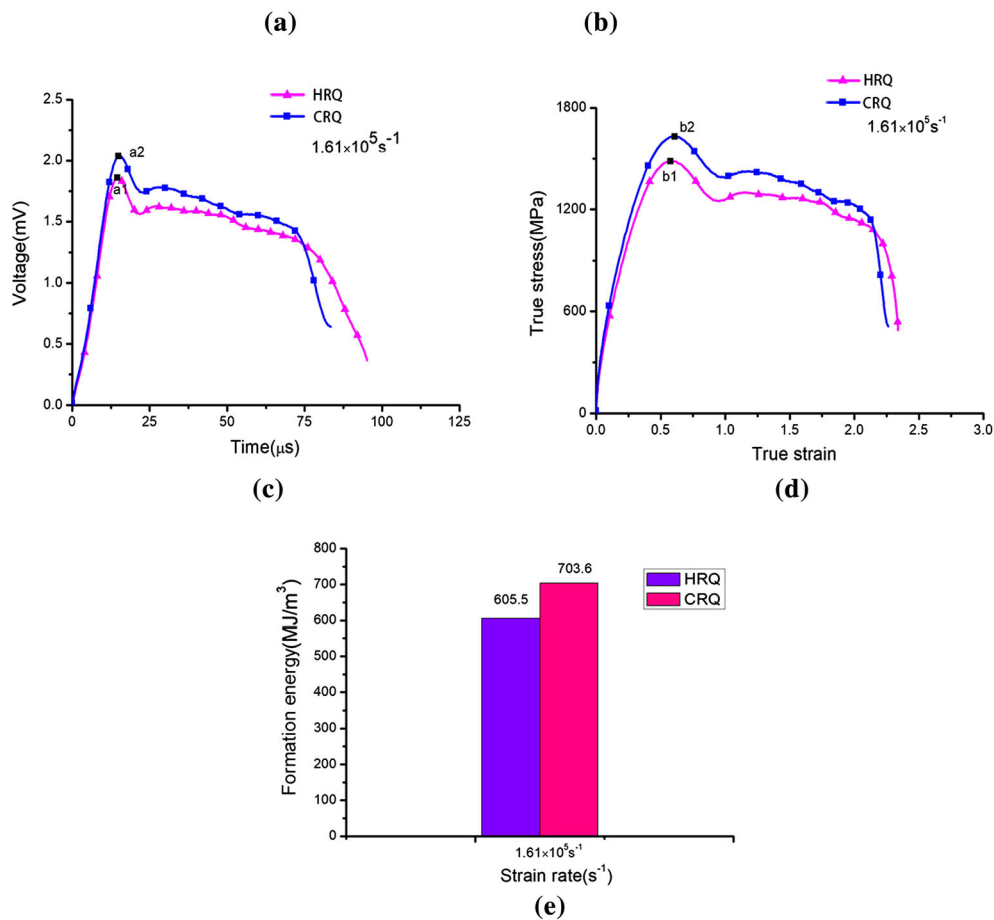
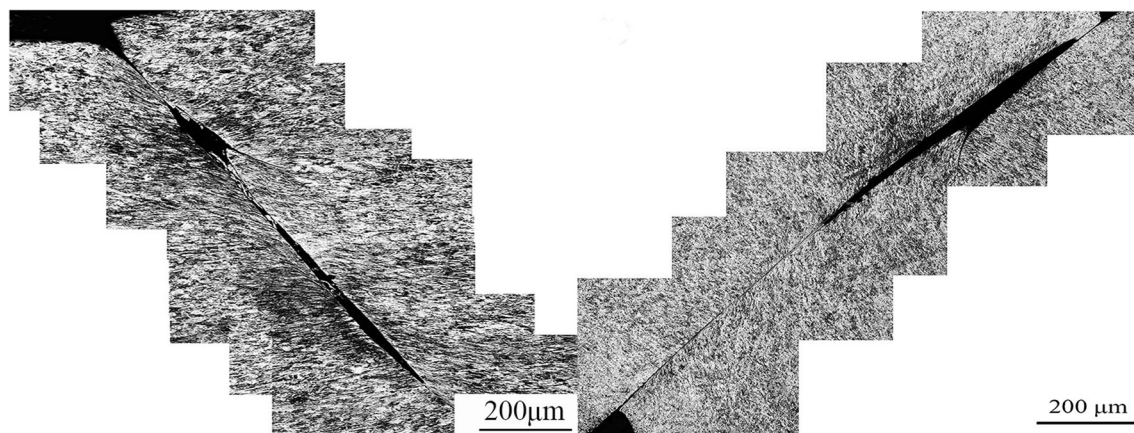


Fig. 5—The comparison of morphological characteristics, loading curves, and formation energy of adiabatic shearing per unit volume of both samples under the loading strain rate of  $1.61 \times 10^5 \text{ s}^{-1}$ : (a) the HRQ sample; (b) the CRQ sample; (c) voltage–time loading curves; (d) true stress–true strain curves; (e) comparison of adiabatic shearing formation energy per unit volume.

Table III that the values of the stress collapse time, the critical strain, and the adiabatic shearing formation energy per unit volume in the HRQ sample are all smaller than those in the CRQ sample under the loading strain rate of  $1.61 \times 10^5 \text{ s}^{-1}$ , which show that the HRQ sample is easier to produce adiabatic shearing localization. In conclusion, the adiabatic shear susceptibility of the HRQ sample is higher than that of the CRQ sample under the same dynamic loading condition. Adiabatic shearing of materials under impact loading can be attributed to the thermal-viscoplastic constitutive instability of the material. The thermal-viscoplastic constitutive equation in the case of one-dimensional shear can be written as<sup>[14]</sup>

$$\tau = f(\gamma, \dot{\gamma}, T) \quad [9]$$

where  $\tau$  is the shear stress,  $\gamma$  is the shear strain,  $\dot{\gamma}$  is the shear strain rate, and  $T$  is the deforming temperature. The critical condition for constitutive instability  $\frac{d\tau}{d\gamma} = 0$  is<sup>[14]</sup>

$$\frac{d\tau}{d\gamma} = \frac{\partial\tau}{\partial\gamma} + \frac{\partial\tau}{\partial\dot{\gamma}} \frac{d\dot{\gamma}}{d\gamma} + \frac{\partial\tau}{\partial T} \frac{dT}{d\gamma} = 0. \quad [10]$$

Adiabatic shearing localization occurred when  $\frac{d\tau}{d\gamma} < 0$ . It can be seen from Eq. [10] that the occurrence of constitutive instability generally depends on the balance between strain hardening of the material  $\frac{\partial\tau}{\partial\gamma}$  ( $> 0$ ), strain rate hardening  $\frac{\partial\tau}{\partial\dot{\gamma}}$  ( $> 0$ ), and thermal softening  $\frac{\partial\tau}{\partial T}$  ( $< 0$ ). The larger the thermal softening effect, the smaller the strain hardening and strain rate hardening effect, the more likely  $\frac{d\tau}{d\gamma}$  is to be less than 0, and the more likely adiabatic shearing localization occurs. In general, low strain hardening, low strain rate hardening, and high thermal softening are conducive to the formation of the adiabatic shear band.<sup>[14]</sup> Li *et al.*<sup>[13,43,44]</sup> studied the effects of grain size and martensite content on the deformation behavior of the Fe<sub>50</sub>Mn<sub>30</sub>Co<sub>10</sub>Cr<sub>10</sub> HEA, and they found that the work hardening effect of samples with fine grain size was greater than that of samples with coarse grain size. According to the analysis in Figure 2, the grain size of the CRQ sample (10  $\mu\text{m}$ ) is smaller than that of the HRQ sample (35  $\mu\text{m}$ ), so the strain hardening effect of the CRQ sample is larger than that of the HRQ sample under the same loading condition. At the same time, the strain rate sensitivity of the material is related to the grain size. The smaller the crystal grains, the strain rate sensitivity of the fcc crystal increases, that is, the strain rate hardening effect increases.<sup>[45]</sup> The CRQ sample of the Fe<sub>50</sub>Mn<sub>30</sub>Co<sub>10</sub>Cr<sub>10</sub> HEA with fcc as the matrix has smaller grain size than the HRQ sample, and the strain rate hardening rate of

the CRQ sample, *i.e.*, strain rate hardening effect  $\left(\frac{\partial\tau}{\partial\dot{\gamma}}\right)$  is larger than that of the HRQ sample. Li *et al.*<sup>[13,43,44]</sup> found that the higher the martensite content before deformation when the grain size of samples was similar, the greater the resistance of the fcc matrix to plastic deformation and the higher the work hardening rate. According to the XRD analysis results (Figure 2), the martensite content (46.0 wt pct) of the CRQ sample is greater than that of the HRQ sample (28.3 wt pct), so the work hardening effect of the CRQ sample is higher than that of the HRQ sample under the same loading condition. In addition, the smaller the grain size and the higher the martensite content, the greater the resistance to plastic failure of the samples.<sup>[13,43,44]</sup> Therefore, the greater the resistance to plastic failure of the CRQ sample was than that of the HRQ sample. Therefore, the strain hardening effect, strain rate hardening effect, and the resistance to plastic failure of the CRQ sample are larger than that of the HRQ sample under the same dynamic loading conditions, indicating that adiabatic shearing is less likely to occur, and the adiabatic shear susceptibility of the CRQ sample is lower.

## 2. Effects of strain rate on the adiabatic shear susceptibility

As shown in Figure 3, there was no adiabatic shear band formed in both samples under the loading strain rate of  $1.37 \times 10^5 \text{ s}^{-1}$  but an adiabatic shear band was formed under the loading strain rate of  $1.55 \times 10^5$  and  $1.61 \times 10^5 \text{ s}^{-1}$  (Figures 4 and 5), and the dynamic damage in both samples became more serious with increasing the loading strain rate, which show that the adiabatic shear susceptibility of both samples increased with higher loading strain rate. The parameters that can characterize the adiabatic shear susceptibility are shown in Tables II and III. As shown in Tables II and III, stress collapse appears earlier in both samples when strain rate increases. At the same time, the critical strain and the adiabatic shearing formation energy per unit volume of both samples decreases with the increase of strain rate. Therefore, the adiabatic shear susceptibility of the sample increases when loading strain rate is higher.

A certain energy barrier was needed to cross to form an adiabatic shear band, and the higher the energy barrier, the more difficult the adiabatic shearing occurs. Grady<sup>[46]</sup> proposed an equation for calculating energy barriers:

$$\Gamma = \sqrt{3} \left( \frac{\rho c}{\alpha} \right) \left( \frac{\rho^3 c^2 \lambda^3}{\tau_y^3 \alpha \dot{\epsilon}} \right)^{\frac{1}{4}}, \quad [11]$$

**Table III. Parameters Characterizing the Adiabatic Shear Susceptibility Under the Loading Strain Rate of  $1.61 \times 10^5 \text{ s}^{-1}$**

	Loading Strain Rate ( $\text{s}^{-1}$ )	Stress Collapse Time ( $\mu\text{s}$ )	Critical Strain	Formation Energy ( $\text{MJ}/\text{m}^3$ )
HRQ	$1.61 \times 10^5$	14.5	0.58	605.5
CRQ	$1.61 \times 10^5$	14.9	0.61	703.6



where  $\rho$  is the material density, and  $c$  is the specific heat capacity.  $\alpha$  is the thermal softening coefficient.  $\lambda$  is the thermal conductivity,  $\tau_y$  is the yield stress, and  $\dot{\epsilon}$  is the strain rate. The higher energy barrier means that the adiabatic shear band is more difficult to form. Strain rates of  $1.37 \times 10^5$ ,  $1.55 \times 10^5$ , and  $1.61 \times 10^5 \text{ s}^{-1}$  were substituted into Eq. [11], and it can be obtained that  $\Gamma_{1.61 \times 10^5}^5 / \Gamma_{1.55 \times 10^5}^5 = 0.98$ ,  $\Gamma_{1.55 \times 10^5}^5 / \Gamma_{1.37 \times 10^5}^5 = 0.94$ , which are both lower than 1, indicating that the higher the strain rate, the lower the energy barrier. Therefore, the adiabatic shear susceptibility of the material increases with increased strain rate.

#### IV. CONCLUSIONS

Effects of microstructures and loading strain rates on the adiabatic shear susceptibility of the Fe<sub>50</sub>Mn<sub>30</sub>Co<sub>10</sub>Cr<sub>10</sub> HEA were analyzed for the first time by comparing the metallographic observation, the stress collapse time, the critical strain corresponding to the adiabatic shearing initiation, and the adiabatic shearing formation energy per unit volume. The findings provide experimental data and theoretical support for the engineering application of this alloy in the dynamic loading field. The conclusions are as follows:

- (1) The adiabatic shear band was not formed in both samples under the loading strain rate of  $1.37 \times 10^5 \text{ s}^{-1}$ , while an adiabatic shear band was formed in both samples under the loading strain rate of  $1.55 \times 10^5$  and  $1.61 \times 10^5 \text{ s}^{-1}$ . For samples possessing the same structure, the higher the strain rate, the more likely the adiabatic shear localization occurs, and the higher the adiabatic shear susceptibility.
- (2) The stress collapse time, the critical strain corresponding to the adiabatic shearing initiation, and the energy absorbed for the formation of the adiabatic shear band of the HRQ sample are lower than those of the CRQ sample under the same dynamic loading condition. The average width of the adiabatic shear band of the HRQ sample is greater than that of the CRQ sample, which indicates that the HRQ sample has a higher adiabatic shear susceptibility. The smaller the grain size and the more the hcp phase of the Fe<sub>50</sub>Mn<sub>30</sub>Co<sub>10</sub>Cr<sub>10</sub> HEA, the larger the strain hardening effect and strain rate strengthening effect and the stronger the localized deformation resistance, and the smaller the adiabatic shear susceptibility under high strain rate loading.

#### ACKNOWLEDGMENTS

This work is supported by the National Natural Science Foundation of China (Nos. 51871243, 51574290) and Hunan Provincial Natural Science Foundation of China (No. 2019JJ40381).

#### REFERENCES

1. B. Cantorb, I.T.H. Chang, and P. Knight: *Mater. Sci. Eng. A*, 2004, vols. 375–377, pp. 213–18.
2. A.J. Zaddach, C. Niu, C.C. Koch, and D.L. Irving: *JOM*, 2013, vol. 65, pp. 1780–89.
3. C.J. Tong, Y.L. Chen, J.W. Yeh, S.J. Lin, S.K. Chen, T.T. Shun, C.H. Tsau, and S.Y. Chang: *Metall. Mater. Trans. A*, 2005, vol. 36A, pp. 881–93.
4. J.W. Yeh: *JOM*, 2013, vol. 65, pp. 1759–71.
5. Y. Zhang and W.J. Peng: *Procedia Eng.*, 2012, vol. 27, pp. 1169–78.
6. Y.F. Ye, Q. Wang, J. Lu, C.T. Liu, and Y. Yang: *Mater. Today*, 2016, vol. 19, pp. 349–62.
7. F. Otto, Y. Yang, H. Bei, and E.P. George: *Acta Mater.*, 2013, vol. 61, pp. 2628–38.
8. S. Basu, Z. Li, K.G. Pradeep, and D. Raabe: *Front. Mater.*, 2018, vol. 5, pp. 1–10.
9. M.J. Yao, K.G. Pradeep, C.C. Tasan, and D. Raabe: *Scripta Mater.*, 2014, vols. 72–73, pp. 5–8.
10. K.G. Pradeep, C.C. Tasan, M.J. Yao, Y. Deng, H. Springer, and D. Raabe: *Mater. Sci. Eng. A*, 2015, vol. 648, pp. 183–92.
11. Y. Deng, C.C. Tasan, K.G. Pradeep, H. Springer, A. Kostkaa, and D. Raabe: *Acta Mater.*, 2015, vol. 94, pp. 124–33.
12. O.N. Senkov, G.B. Wilks, D.B. Miracle, C.P. Chuang, and P.K. Liaw: *Intermetallics*, 2010, vol. 18, pp. 1758–65.
13. Z.M. Li, K.G. Pradeep, Y. Deng, D. Raabe, and C.C. Tasan: *Nature*, 2016, vol. 534, pp. 227–30.
14. M.A. Meyers: *Dynamic Behavior of Materials*, Wiley, New York, 1994.
15. M.A. Meyers, Y.B. Xu, Q. Xue, M.T. Perez-Prado, and T.R. McNelley: *Acta Mater.*, 2003, vol. 51, pp. 1307–25.
16. Q. Xue and G.T. Gray: *Metall. Mater. Trans. A*, 2006, vol. 37A, pp. 2435–46.
17. Y. Yang, X.L. Lian, and J.L. Wang: *J. Mater. Sci.*, 2019, vol. 54, pp. 7256–70.
18. Y.B. Xu, W.L. Zhong, Y.J. Chen, L.T. Shen, Q. Liu, Y.L. Baic, and M.A. Meyers: *Mater. Sci. Eng. A*, 2001, vol. 299, pp. 287–95.
19. G.M. Owolabi, D.T. Bolling, A.A. Tihamiyu, R. Abua, A.G. Odeshi, and H.A. Whitwortha: *Mater. Sci. Eng. A*, 2016, vol. 655, pp. 212–20.
20. J. Peirs, W. Tirry, B. Amin-Ahmadi, F. Coghe, P. Verleysen, L. Rabet, D. Schryvers, and J. Degrieck: *Mater. Charact.*, 2013, vol. 75, pp. 79–92.
21. Y. Yang and B.F. Wang: *Mater. Lett.*, 2006, vol. 60, pp. 2198–2202.
22. B.F. Wang and Y. Yang: *Mater. Sci. Eng. A*, 2008, vol. 473, pp. 306–11.
23. Y. Yang, F. Jiang, B.M. Zhou, X.M. Li, H.G. Zheng, Q.M. Zhang, and Y.Q. Zhao: *Mater. Sci. Eng. A*, 2011, vol. 528, pp. 2787–94.
24. Y. Yang, X.M. Zhang, Z.H. Li, and Q.Y. Li: *Acta Mater.*, 1996, vol. 44, pp. 559–65.
25. L. Zhen, D.L. Zou, C.Y. Xu, and W.Z. Shao: *Mater. Sci. Eng. A*, 2010, vol. 527, pp. 5728–33.
26. Y. Yang and L.H. Jiang: *Mater. Sci. Eng. A*, 2016, vol. 664, pp. 146–54.
27. Y. Yang and L.H. Jiang: *Mater. Sci. Eng. A*, 2016, vol. 655, pp. 321–30.
28. Y. Yang, L.H. Jiang, Z. Xu, and Z. Wang: *Mater. Sci. Eng. A*, 2017, vol. 685, pp. 57–64.
29. Y. Yang, S.J. Yang, and L.H. Jiang: *Mater. Character.*, 2019, vol. 156, art. no. 109840, <http://doi.org/10.1016/j.matchar.2019.109840>.
30. J.R. Li, J.L. Yu, and Z.G. Wei: *Int. J. Impact Eng.*, 2008, vol. 28, pp. 303–14.
31. D. Rittel and R. Levin: *Mech. Mater.*, 1998, vol. 30, pp. 197–216.
32. L.H. Dai, L.F. Liu, and Y.L. Bai: *Int. J. Solids Struct.*, 2004, vol. 41, pp. 5979–93.
33. M.N. Bassim and N. Panic: *J. Mater. Process. Tech.*, 1999, vol. 92, pp. 481–85.
34. Y. Yang, G.Y. Tan, P.X. Chen, and Q.M. Zhang: *Mater. Sci. Eng. A*, 2012, vol. 546, pp. 279–83.
35. W.D. Songa, M.L. Hua, H.S. Zhang, and Y.X. Jin: *Mater. Sci. Eng. A*, 2018, vol. 725, pp. 76–87.

36. W.S. Lee, T.H. Chen, and G.T. Liu: *Metal Sci. J.*, 2013, vol. 26, pp. 720–25.
37. Y. Yang, L.H. Jiang, S.H. Luo, H.B. Hu, T.G. Tang, and Q.M. Zhang: *J. Mater. Eng. Perform.*, 2016, vol. 25, pp. 29–37.
38. N. Kumar, Q. Ying, X. Nie, R.S. Mishra, Z. Tang, and P.K. Liaw: *Mater. Design*, 2015, vol. 86, pp. 598–602.
39. Z. Li, S. Zhao, H. Diao, P.K. Liaw, and M.A. Meyers: *Nature*, 2017, vol. 7, pp. 1–8.
40. Z.Z. Li, S.T. Zhao, S.M. Alotaibi, Y. Liu, B.F. Wang, and M.A. Meyers: *Acta Mater.*, 2018, vol. 151, pp. 1–23.
41. S.J. Yang, Y. Yang, and H.M. Wang: *Adv. Eng. Mater.*, 2019, <https://doi.org/10.1002/adem.201900868>.
42. P. Haušild, V. Davydov, J. Drahokoupil, M. Landa, and P. Pilvin: *Mater. Design*, 2010, vol. 31, pp. 1821–27.
43. S. Basu, Z.M. Li, K.G. Pradeep, and D. Raabe: *Frontiers in Mater.*, 2018, vol. 5, pp. 1–10.
44. Z.M. Li, C.C. Tasan, K.G. Pradeep, and D. Raabe: *Acta Mater.*, 2017, vol. 131, pp. 323–35.
45. Y.Z. Guo, Y.L. Li, Z. Pan, F.H. Zhou, and Q. Wei: *Mech. Mater.*, 2010, vol. 42, pp. 1020–29.
46. D.E. Grady: *Mech. Mater.*, 1994, vol. 17, pp. 289–93.

**Publisher's Note** Springer Nature remains neutral with regard to jurisdictional claims in published maps and institutional affiliations.